Conformational Plasticity in the Selectivity Filter of the TRPV2 Ion Channel

Lejla Zubcevic[1], **Son Le**[1], **Huanghe Yang**[1,2], and **Seok-Yong Lee**[1,*]

[1]Department of Biochemistry, Duke University School of Medicine, Durham, North Carolina, 27710, USA

[2]Department of Neurobiology, Duke University School of Medicine, Durham, North Carolina, 27710, USA

Summary

Transient receptor potential vanilloid (TRPV) channels are activated by ligands and heat, and are involved in various physiological processes. In contrast to the architecturally-related voltage-gated cation channels, TRPV1 and TRPV2 subtypes possess another activation gate at the selectivity filter that can open widely enough to permeate large organic cations. Despite the advances in recent structural studies, the mechanism of selectivity filter gating and permeation of both metal ions and large molecules by TRPV1 or TRPV2 is not well known. We determined two crystal structures of rabbit TRPV2 in its Ca^{2+}-bound and resiniferatoxin (RTx) and Ca^{2+}-bound forms to 3.9 Å and 3.1 Å, respectively. Notably, our structures show that RTx binding leads to two-fold symmetric opening of the selectivity filter of TRPV2 that is wide enough for large organic cation permeation. Combined with functional characterizations, our studies reveal a structural basis for permeation of Ca^{2+} and large organic cations in TRPV2.

The vanilloid transient receptor potential (TRPV) channel family, part of the TRP channel superfamily, is composed of six members, TRPV1-TRPV6, which are involved in various physiological processes including nociception, osmosensation, and Ca^{2+} regulation [1–4]. Two members of this family, TRPV1 and TRPV2, are activated by natural products including capsaicin and cannabinoids as well as heat [5,6]. The question of how TRPV1 and TRPV2 increase their Ca^{2+} conductance in response to physical and chemical stimuli has been at the center of the field since their discovery [7]. Although they are architecturally related to canonical voltage-gated cation channels, a crucial distinction exists in that TRPV1 and TRPV2 possess two activation gates: one at the selectivity filter (the SF gate) and the other one at the S6 helical bundle crossing at the intracellular mouth of the pore (the common gate). This is in stark contrast with canonical voltage-gated cation channels which contain

the common gate as the only activation gate [8–13]. A recent structure of the TRPV1 channel in complex with the doubleknot toxin (DkTx) and resiniferatoxin (RTx) has provided us with a better understanding of how binding of these toxins in the vicinity of the SF gate and the common gate, respectively, leads to opening of both gates [14]. However, many questions still remain unanswered. Firstly, several TRPV channels (TRPV1, TRPV2, TRPA1) have been shown to permeate large organic cationic molecules (up to ~400 Da), which are much larger than metal ions [15–22]. This phenomenon, initially termed "pore dilation", was thought to occur through gradual change in the selectivity filter upon repeated stimulation [16,19]. While this model of dynamic changes in the selectivity during gating has since been challenged [17,23,24], the ability of some TRPV channels to permeate large organic cations is well established and has been exploited as a mechanism for delivery of small molecule drugs[17,20,25–27]. However, the structural basis for this phenomenon remains elusive since a structure of a fully open SF gate has not been captured to date. Common gate opening in several ion channels has been shown to be large enough to pass large organic cations [8,28–30]. Secondly, the mechanism of Ca^{2+} recognition in the SF of TRPV1 and TRPV2 is not known, as ions were not resolved in any of the structures reported to date [31–33]. Thirdly, because previous studies of TRPV1 used both DkTx and RTx to open the SF gate and the common gate, it is not clear how binding of the vanilloid toxin RTx at the inner leaflet of the membrane opens the SF gate of TRPV1 in the absence of DkTx. Finally, until now all the structural studies of the TRP channels have had four-fold (C4) symmetric conformations but whether the channel gating involves less symmetric or asymmetric (C2 or C1) arrangements within the tetramer has not been clear, as asymmetric TRPV channel structures have not been captured.

To address these issues and study the mechanism of ligand-dependent TRPV2 activation, we have performed structural studies of TRPV2. TRPV2 shares a high sequence identity with TRPV1 (~50%), and is activated by heat, cannabinoids and 2-aminoethoxydiphenyl borate (2-APB) but not by RTx. Recently, two groups independently showed that introduction of four point mutations rendered TRPV2 sensitive to RTx, thereby demonstrating the conserved mechanism of ligand-dependent activation of TRPV1 and TRPV2 [34,35].

Here we present two crystal structures of TRPV2 in its Ca^{2+}-bound form and RTx and Ca^{2+} bound form at 3.9 Å and 3.1 Å, respectively (Fig. 1a, Supplementary Table 1). Through structural analysis combined with functional studies, we have identified novel structural arrangements of the SF gate of TRPV2 elicited by RTx binding that enables permeation of large cations.

Crystal structures of TRPV2 in the presence and absence of RTx

For structure determination, we utilized the minimal TRPV2 construct (miTRPV2) from the rabbit, *Oryctolagus cuniculus,* similar to those used for cryo-EM studies of rabbit TRPV2 and rat TRPV1 (48% sequence identity to rat TRPV1, see methods and Supplementary Fig. 1) [31,32]. We previously showed that both wild-type TRPV2 and miTRPV2 are activated by 2-APB by Ca^{2+} imaging and whole cell patch-clamp recording experiments [32]. We introduced four point mutations (Phe470Ser, Leu505Met, Leu508Thr and Gln528Glu; TRPV2$_{QM}$) into wtTRPV2 and miTRPV2 as reported [34] and tested the sensitivity of the

constructs to RTx. Our inside-out and whole-cell patch clamp recordings showed that both wtTRPV2$_{QM}$ and miTRPV2$_{QM}$ exhibited RTx-dependent currents that were slow and irreversible while the control TRPV2 constructs were not sensitive to RTx (Fig. 1c–d, Supplementary Fig. 2). Both TRPV2$_{QM}$ and miTRPV2$_{QM}$ are blocked by 200 μM Ruthenium Red (RuR) from both sides of the membrane in the inside-out configuration: RuR completely blocks outward currents of TRPV2$_{QM}$ when introduced to the cytosolic side of the excised patch (Fig. 1c–d) and blocks inward currents when introduced to the pipette solution (Supplementary Fig. 2). In the whole-cell configuration, RuR substantially reduces TRPV2 currents when introduced to the extracellular solution (Supplementary Fig. 2). Both TRPV2$_{QM}$ and miTRPV2$_{QM}$ still can be activated by 2-APB (Supplementary Fig. 2), suggesting that introducing a separate RTX binding site does not interfere with 2-APB binding to the TRPV2 channels.

Both miTRPV2 alone and miTRPV2$_{QM}$ in complex with RTx were crystallized under similar conditions in the presence of Ca^{2+} (see Methods). The crystal structures of miTRPV2 in the presence of Ca^{2+} (referred to as miTRPV2$_{Ca^{2+}}$) and miTRPV2$_{QM}$ in complex with RTx in the presence of Ca^{2+} (referred to as miTRPV2$_{RTx,Ca^{2+}}$) were determined to 3.9 Å and 3.1 Å, respectively. Molecular replacement was employed for phasing using fragments of the cryo-EM structure of miTRPV2 (miTRPV2$_{EM}$, PDB ID: 5AN8) as search models. The model building was guided by anomalous difference Fourier maps obtained from the structure of selenomethionine-labelled miTRPV2$_{Ca^{2+}}$ (Supplementary Fig. 3). The models were built and refined to a good overall geometry (Supplementary Table 1).

Both structures exhibit the well-established TRPV channel fold where the four protomers with six transmembrane helices (S1-S6) form a domain-swapped homotetramer with each voltage-sensor like domain (VLSD, S1-S4) interacting with the pore domain (S5-S6) of its neighboring protomer with the S4-S5 helix (S4-S5 linker) mediating this domain-swapped configuration (Fig. 1). The higher-resolution crystal structure of miTRPV2$_{RTx,Ca^{2+}}$ enabled a more complete model building than the miTRPV2$_{EM}$ structure [32]. Notably, both N-terminal ankyrin repeat domain (ARD) and the C-terminal domain (CTD), which were not well resolved in previous TRPV1 and TRPV2 structures [14,31–33,36], are almost fully resolved in the electron density map (Supplementary Figs. 3 and 4). All four RTx binding sites are occupied in the structure of miTRPV2$_{RTx,Ca^{2+}}$, as shown in F_O-F_C simulated annealing omit map (Supplementary Fig. 5). Interestingly, the top-down view shows that both miTRPV2$_{Ca^{2+}}$ and miTRPV2$_{RTx,Ca^{2+}}$ structures reveal two-fold symmetric arrangement within the homotetramer, a marked contrast with that of the miTRPV2$_{EM}$ structure (Fig. 1b).

The π-helix in the S4-S5 linker determines the subunit arrangement of

$miTRPV2_{Ca^{2+}}$

We first compared the structures of $miTRPV2_{Ca^{2+}}$ and $miTRPV2_{EM}$, and found that while the dimensions of the cytoplasmic ankyrin repeat domains (ARDs) remain unchanged, the dimensions of the two membrane channel regions are different: $miTRPV2_{Ca^{2+}}$ is contracted at the extracellular side of the membrane by ~13 Å along one direction (y-axis) and ~6 Å along the other direction (x-axis) compared to $miTRPV2_{EM}$ (measured using Cα of Asn429 at the top of opposing S2 helices), leading to a two-fold symmetric structural arrangement in the channel region of $miTRPV2_{Ca^{2+}}$ (Fig. 2a). Two-fold symmetric arrangements of TRP channels have never been observed before. Because of the domain-swapped configuration, each subunit is composed of VSLD of one polypeptide chain and the pore domain of the neighboring chain, and the S4-S5 linker connects one subunit to the adjacent subunit. Structural analyses revealed that the contraction of $miTRPV2_{Ca^{2+}}$ along the y axis with respect to $miTRPV2_{EM}$ is caused by a ~7° rigid body rotation of the entire subunit around an axis formed by the S4-S5 linker and the S4b (Fig. 2b). Superposition of each subunit of $miTRPV2_{Ca^{2+}}$ with the subunit of $miTRPV2_{EM}$ reveals that the VSLD (S1-S4) and the pore domain (S5-S6) align well (Cα r.m.s.d. of 0.75 Å), while the S4-S5 linker and the pore helix exhibit large conformational changes (Fig. 2b–d).

Based on structural comparisons of the TRPV1 and TRPV2 cryo-EM structures, it has been proposed that a π-helix, a rare helix with a wider turn than an α-helix (4.1 vs. 3.6 residues per turn), plays an important role in TRPV channel gating by introducing a hinge in the key helices [32] and recent structural studies showed that this α-to-π-helical transition indeed occurs in S6 of TRPV6 [37]. While the S4-S5 linker and S5 in $miTRPV2_{EM}$ form a continuous α-helical structure, $miTRPV2_{Ca^{2+}}$ contains a π-helix between the S4-S5 linker and S5 helices (termed π-hinge$_{S4-S5}$). Notably, the two-fold symmetric $miTRPV2_{Ca^{2+}}$ contains π-hinges$_{S4-S5}$ at two different positions. While the more contracted subunit has a π-hinge$_{S4-S5}$ beginning at Asp534, the less contracted subunit contains a π-hinge$_{S4-S5}$ that begins at Ile531. This difference in the π-hinge positions results in different angles between the S4-S5 linker and S5 and therefore in different degrees of subunit rotation which is responsible for the two-fold symmetric rearrangements (Fig. 2d). The two-fold symmetric contraction of $miTRPV2_{Ca^{2+}}$ near the extracellular region leads to pore helix rearrangements with ~7.5° angle tilt and ~3.5 Å outward displacement compared to $miTRPV2_{EM}$ (Fig. 2c).

RTx binding leads to two-fold symmetric rearrangement of the TRPV2 channel

Although all four subunits are bound to RTx in the structure of miTRPV2$_{RTx,Ca^{2+}}$, (Fig. 1a and Supplementary Fig. 5) the channel region of miTRPV2$_{RTx,Ca^{2+}}$ exhibits a widening along only one dimension (the x-axis) near the extracellular side by ~7 Å with respect to miTRPV2$_{Ca^{2+}}$ (Fig. 2e). Notably, the widening in subunits A and C results in a novel arrangement of the SF gate. Upon a rigid body rotation around the π-hinge$_{S4-S5}$, the subunits of miTRPV2$_{RTx,Ca^{2+}}$ and miTRPV2$_{Ca^{2+}}$ aligned well (Cα r.m.s.d.=0.99 Å) with only the S4-5 linker and the pore helix deviating significantly (Supplementary Fig. 5). In the structure of miTRPV2$_{RTx,Ca^{2+}}$, the position of π-hinge$_{S4-S5}$ in all four subunits is the same, but two diagonally positioned subunits (A and C) assume a hinge orientation and angle between the S4-S5 linker and S5 which is distinct from the other two subunits (B and D), giving rise to the two-fold symmetric pore conformation (Fig. 2e–f). The RTx binds in a pocket formed by S3, S4b, the S4-S5 linker S5 and S6. However, its interactions with the pocket are different in the two adjacent subunits of miTRPV2$_{RTx,Ca^{2+}}$, and this difference in RTx binding appears to induce different hinge orientations and subunit arrangements and ultimately result in the two-fold symmetric widening of the SF gate in the structure of miTRPV2$_{RTx,Ca^{2+}}$ (Supplementary Fig. 5).

Structural comparison of miTRPV2$_{RTx,Ca^{2+}}$ with miTRPV2$_{EM}$ shows that two subunits are widened by ~2 Å along one direction (the x-axis) and two subunits are contracted by ~7 Å along the other direction (the y-axis) near the extracellular side with respect to miTRPV2$_{EM}$ (Supplementary Fig. 6a). When the subunits of the miTRPV2$_{RTx,Ca^{2+}}$ were superposed to the subunit of miTRPV2$_{EM}$, the VSLD and the S5 and S6 aligned well (Cα r.m.s.d=0.61 Å), but there was a substantial divergence in the pore helix and the S4-5 linker (Supplementary Fig. 6). There is a ~19° difference in the angle of the two pore helices as well as ~3.5 Å outward shift in the pore helix of miTRPV2$_{RTx,Ca^{2+}}$, suggesting that the pore helix conformation is dependent on the conformation of the S4-S5 linker and the resulting subunit arrangement within the pore (Supplementary Fig. 6).

RTx binding leads to a wide, two-fold symmetric opening of the selectivity filter gate

A structural comparison of the channel regions of miTRPV2$_{EM}$, miTRPV2$_{Ca^{2+}}$, and miTRPV2$_{RTx,Ca^{2+}}$ shows that while the pore helices in miTRPV2$_{EM}$ are arranged in a four-fold symmetric manner around the pore, and this four-fold symmetry is to some extent preserved in miTRPV2$_{Ca^{2+}}$ through concerted rearrangement of pore helices, the pore

helices of miTRPV2$_{RTx,Ca^{2+}}$ are positioned in a distinctly 2-fold symmetric manner around the ion permeation path (Fig. 3a). A closer look at the pore-lining components, S6 and the pore helix, of the widened subunits (A and C) and the contracted subunits (B and D) further illustrates the conformational changes of the pore upon RTx binding (Fig. 3b–c). In the miTRPV2$_{EM}$ structure, the SF gate is tightly closed, as the distance between diagonally positioned Gly604 carbonyl oxygens is 5.2 Å. In the structure of miTRPV2$_{Ca^{2+}}$, the corresponding distances between Gly604 carbonyl oxygens are 6.1–6.4 Å. Here we observe an electron density peak, which we tentatively assigned as Ca^{2+} given that Na^{+} is difficult to observe at this resolution. Although the quality of the electron density map around the pore made unambiguous assignment of the pore helices in miTRPV2$_{Ca^{2+}}$ difficult, the carbonyls of Ile603 appear to coordinate the Ca^{2+} ion via water molecules. In the contracted subunits (B and D) of the miTRPV2$_{RTx,Ca^{2+}}$ structure, the distance between the Gly604 carbonyl oxygens is increased to ~7.1 Å and two putative Ca^{2+} ions are present in the pore: one in the SF and the other one in the cavity. Notably, the high-resolution structure reveals a novel mode of coordination of the Ca^{2+} ion in the SF: two pore helices are aligned in a way which allows the helical dipole to be utilized in coordinating the ion in the SF, as carbonyls of Phe601, Thr602 and Ile603, located at the C-termini of the pore helices from the two contracted subunits, are in a position to make water-mediated coordination of the Ca^{2+} ion in the SF (Figs. 3b and 3d). Strikingly, in widened subunits (A and C) of the miTRPV2$_{RTx,Ca^{2+}}$, the distance between the Ile603 carbonyls increases to ~12.3 Å (Fig. 3c). Thus, these two subunits are not involved in ion coordination. Although only two subunits are involved, six carbonyl atoms are within range to participate in coordination of the semi-hydrated calcium ion in the SF (Fig. 3d). The cavity of miTRPV2$_{RTx,Ca^{2+}}$ is hydrophobic and Tyr632 is the only polar amino acid in the cavity. Hydroxyl groups of Tyr632 from the two contracted subunits of miTRPV2$_{RTx,Ca^{2+}}$ are ~6 Å away from the cavity ion, making these two residues likely candidates for water-mediated coordination of the cavity ion (Fig. 3b). An additional density peak was observed in the cavity near the cavity ion of the miTRPV2$_{RTx,Ca^{2+}}$ which could not be assigned to polypeptide or ions (Supplementary Fig. 4). The common gate of the miTRPV2$_{RTx,Ca^{2+}}$ is slightly more open than miTRPV2$_{EM}$ but its opening is not wide enough to permeate hydrated Ca^{2+} ions, suggesting that only the SF gate is open in the miTRPV2$_{RTx,Ca^{2+}}$ structure (Supplementary Fig. 6).

The wide opening at the SF gate in the miTRPV2$_{RTx,Ca^{2+}}$ structure suggests that, in this state, the channel could permeate molecules much larger than small metal ions such as Na^{+}, K^{+} and Ca^{2+}. Therefore, this finding might represent the first observation of a fully open SF gate that is permeable to large organic cations. To test whether full-length TRPV2$_{QM}$ and miTRPV2$_{QM}$ are able to permeate large organic cations, we expressed the constructs in HEK293 cells and measured the uptake of the fluorescent molecule YO-PRO-1 (M.W. 376Da) upon application of RTx. We observed that YO-PRO-1 was rapidly taken up by the

full-length $TRPV2_{QM}$ and $miTRPV2_{QM}$ expressing cells, which is consistent with previous reports on YO-PRO-1 permeation in TRPV1 (Fig. 4a–b) [15,22]. We also observed YO-PRO-1 uptake by wtTRPV2 and $TRPV2_{QM}$ expressing cells upon application of 2-APB (Supplementary Fig. 2h), indicating that 2-APB can also trigger similar rearrangement of the SF gate to allow YO-PRO-1 ions to go through. However, the 2-APB facilitated YO-PRO-1 uptake is slower than the RTx-induced YO-PRO-1 uptake (Fig. 4a), probably because 2-APB is a weaker agonist for TRPV2 than RTx for $TRPV2_{QM}$. The YO-PRO-1 uptake was completely blocked by 50 μM extracellular RuR (Fig. 4a–b). As RuR is a pore blocker for TRPV2 channels (Fig. 1d), this result indicates that YO-PRO-1 enters the cells through the SF gate of the TRPV2 channels. To further test if YO-PRO-1 directly permeates through the TRPV2 SF gate, we examined the effects of YO-PRO-1 on Na^+ permeation through the TRPV2 channel. When YO-PRO-1 was applied from extracellular side, it reduced inward Na^+ currents in a dose-dependent manner with minimal effect on the outward Na^+ currents and vice versa (Fig. 4c–d and Fig. 5f). It is worth noting that the blockade effect of YO-PRO-1 depends on membrane voltage: the larger the driving force, the stronger the blockade effect. Considering dose- and voltage-dependence of YO-PRO-1 blockade of Na^+ currents through TRPV2 from both sides of the membrane (Fig. 4c–d and Fig. 5f) and its uptake through TRPV2 channel pore (Fig. 4a–b), we conclude that the large cation YO-PRO-1 serves as a permeant pore blocker that can go through the SF gate and compete with smaller metal ions for the permeation pathway of TRPV2. Due to its large size, the permeability of YO-PRO-1 must be low, but it is sufficient to limit Na^+ permeation in our patch clamp recordings and to enable fluorescent labeling of nucleic acids inside the cell in our dye uptake experiment. Taken together, we conclude that large organic cations such as YO-PRO-1 can go through the TRPV2 SF gate that has been opened by RTx.

Two-fold symmetric SF gate widening for YO-PRO-1 permeation

Previous structural studies of TRPV1 have associated RTx primarily with opening of the common gate and DkTx with opening of the SF gate, because of the proximity of these toxin bindings sites to the respective gates [14]. Because our structure only contains RTx, it offers an opportunity to get an insight into the allosteric coupling between RTx binding and gating at the SF. Alignment of the widened subunit of $miTRPV2_{RTx,Ca^{2+}}$ and the corresponding subunit of $miTRPV2_{Ca^{2+}}$ suggests that binding of RTx in this mode is not compatible with $miTRPV2_{Ca^{2+}}$, as it would clash with Leu535 at the base of S5 adjacent to π-$hinge_{S4-S5}$ (Fig. 5a). RTx binding appears to push down on the base of S5 and force the S4-5 linker to bend into a different conformation via the π-$hinge_{S4-S5}$, which results in a rotation and consequent widening of the entire subunit. The RTx molecule in the contracted subunits is bound in a different mode and does not appear to exert the same pressure on the π-$hinge_{S4-S5}$, which would explain why it does not elicit widening of the subunit (Supplementary Fig. 7).

Interestingly, the pore helix of the contracted subunits is supported by a hydrogen bond triad which consists of Tyr542 in S5, Thr602 in the pore helix and Tyr627 in S6. By contrast, the hydrogen bond network at the Tyr542-Thr602-Tyr627 triad is broken in the widened subunit

(Fig. 5b–c). This hydrogen bond triad is also broken in the structure of miTRPV2$_{EM}$, which might account for its distinct pore helix position (Supplementary Fig. 7). Away from the H-bond triad, Tyr632 assumes two distinct conformations in the two subunits of miTRPV2$_{RTx,Ca^{2+}}$. In the contracted subunits, this residue lines the cavity and provides an apparent ion coordination site (Fig. 3b and Fig. 5b), and in the widened subunit, it interacts with the pore helix of the neighboring contracted subunit (Fig. 3c and Fig. 5c).

To test if the conformation observed in the miTRPV2$_{RTx,Ca^{2+}}$ is important for permeation of large molecules, we introduced point mutations to residues Tyr542, Thr602, Tyr627, which form the hydrogen-bond triad, and Tyr632, which lines the cavity, in the full-length TRPV2$_{QM.}$ We tested the effects of the point mutations on the permeation of YO-PRO-1, on the RTx-induced Na$^+$ currents, and the reduction of Na$^+$ current by YO-PRO-1 (Fig. 5d–i). Because we observed that Tyr627Ala mutant does not exhibit any appreciable currents, we excluded it from our subsequent analyses. Intriguingly, the uptake of YO-PRO-1 by the Thr602Ala mutant is significantly reduced and slowed while its apparent Na$^+$ conductance is preserved. Furthermore, the reduction of Na$^+$ currents by YO-PRO-1 is significantly enhanced by the Thr602Ala mutation suggesting that YO-PRO-1 acts more as a blocker rather than a permeant in the Thr602Ala mutant. Notably, Tyr542Ala shows a very similar phenotype as Thr602Ala in its reduced YO-PRO-1 uptake, apparently unperturbed Na$^+$ conductance, and increased reduction of Na$^+$ currents by YO-PRO-1. To further test the effect of the mutations on the large organic cation permeation, we utilized NMDG$^+$, which is smaller than YO-PRO-1 (M.W. 195 Da vs 376 Da), to test if the relative permeability of NMDG$^+$ over Na$^+$ changes upon mutation. Consistent with the observed reduction of Na$^+$ current by YO-PRO-1, the Thr602Ala mutation also reduces the permeability ratio of the large cation NMDG$^+$ over Na$^+$ in the TRPV2$_{QM}$ channel in inside-out patch configuration (Supplementary Fig. 8). These data suggest that the hydrogen bond between the pore helix (Thr602) and S5 (Tyr542) is important for the SF gate conformation that allows for large organic cation permeation such as YO-PRO-1 and NMDG$^+$. These results are seemingly counterintuitive because the hydrogen bond between Thr602 and Tyr542 is present only in the contracted subunits of the miTRPV2$_{RTx,Ca^{2+}}$, yet its disruption preferentially reduces large organic cation permeation by TRPV2. We suggest that this result is indicative of the importance of the two-fold symmetric arrangement of the SF gate in permeating large cations.

The Tyr632Ala mutation exhibited a robust YO-PRO-1 uptake and large sodium currents. However, YO-PRO-1-mediated reduction of Na$^+$ currents was substantially impaired in the Tyr632Ala (Figs. 5d–e, 5f and 5h). This reduction in YO-PRO-1 block in the Tyr632Ala mutant may be caused by an increase in the size or width of the cavity which results from removal of a bulky aromatic residue.

To further probe the importance of a two-fold symmetric SF gate widening in large organic cation permeation, we tested if TRPV2$_{QM}$ can permeate tetrabutylammonium (TBA) ions. TBA is smaller than YO-PRO-1 (242 Da vs 376 Da), but unlike YO-PRO-1 it is a symmetric molecule. We found that TBA blocks TRPV2$_{QM}$ in a manner similar to RuR (Figs. 5g and

5i). This suggests that the pore might open in a two-fold symmetric way during gating and that the TBA ion, despite its smaller size cannot permeate because its symmetric shape is incompatible with the asymmetric opening at the SF gate. The Tyr632Ala mutation significantly impaired the ability of TBA to block the Na^+ current, which is consistent with the impaired block of currents by YO-PRO-1 in this mutant (Figs. 5g and 5i).

In the TRPV1 structures, we found that the corresponding hydrogen-bond triad exists in the closed state of TRPV1 (apoTRPV1) while the hydrogen-bond triad is broken in the open state of TRPV1 (DkTx and RTx-bound TRPV1) (Fig. 6a). The DkTx and RTx-bound TRPV1 pore is slightly expanded compared to apoTRPV1, analogous to the widened subunit of $miTRPV2_{RTx,Ca^{2+}}$. In order to test if these interactions are also important for permeation of large organic cationic molecules in TRPV1, we generated point mutations Thr641Ala and Tyr584Ala and performed the same set of electrophysiological experiments. While Tyr584Ala did not generate appreciable Na^+ currents, we found that Thr641Ala produced robust Na^+ currents. Notably, the uptake of YO-PRO-1 by the Thr641Ala mutant is significantly reduced and slowed but the reduction of Na^+ currents by YO-PRO-1 is enhanced by the mutation, consistent with the effects of the Thr602A mutation in $TRPV2_{QM}$ (Fig. 6b–f)). This data suggests that like in TRPV2, a two-fold symmetric arrangement of subunits in TRPV1 play a role in permeation of large cationic molecules.

Discussion

Here we have shown that the SF gate of TRPV2 can adopt multiple conformations through different symmetrical arrangements in the pore, and that these distinct conformations are associated with differential Ca^{2+} binding in the pore, suggesting that the ion permeation and channel gating is coupled in the TRPV1 and TRPV2 channels through the SF gate.

It is also worth noting that during our crystallization efforts we encountered crystals with two-fold symmetric arrangements of the channel in the absence of Ca^{2+} as well as crystals with a tetragonal space group (a four-fold symmetric arrangement) in the presence of Ca^{2+} (Zubcevic and Lee, unpublished data), suggesting that Ca^{2+} does not play a role in the two-fold symmetric arrangement of the channel in the crystal, and the channel can adopt a four-fold symmetrical conformation in the crystal. Furthermore, the Tyr542-Thr602-Tyr627 triad interactions that we showed are important in the permeation of large cations in TRPV2 has only been observed in the crystal structures of TRPV2, further supporting the physiological relevance of the two-fold symmetric arrangements in TRPV2 permeation and gating. However, we cannot distinguish whether the observed two-fold symmetric arrangement of the SF within the TRPV2 tetramer upon RTx binding represents an open state or an important intermediate state on the conformational path towards a fully open symmetric state for large organic cation permeation. Interestingly, asymmetric gating at the SF has been observed in MD simulations of the TRPV1 channel [38].

Symmetry breaking in channel gating has been reported in structural studies of the homo-oligomeric Mg^{2+} ion channel CorA [39]. However, while CorA assumes an asymmetric open conformation in the absence of its ligand, Mg^{2+}, symmetry breaking in TRPV2 appears to be elicited by ligand binding. How does ligand-induced break (or reduction) in the symmetrical

quaternary structure arrangement in TRPV2 occur? Because TRPV channels adopt a domain-swapped arrangement with the S4-S5 linker joining neighboring subunits, we reasoned that ligand binding to the S4-S5 linker influences the rearrangement of subunits. In the recent cryo-EM structural studies of the Na^+ activated K^+ channel Slo2.2, which is not domain-swapped, MacKinnon and colleagues tracked the structural changes in the conformational ensemble of the Slo2.2 channel upon increasing the concentration of Na^+ [40]. However, they did not observe any reduced symmetric arrangements during the structural transitions, consistent with the idea of the importance of the domain-swapped configuration for reduced symmetric conformational transitions. However, this raises the question why reduced symmetric quaternary structural arrangements during channel gating have never been observed in voltage-gated K^+ (K_v) channels that do adopt a domain-swapped arrangement. We speculate that this distinction between TRPV1 and TRPV2 and K_V channels arises from the differences in design of the dynamic and static regions within these channels: First, the interactions between S5 and S6 (pore domain) and the VSLD within the subunit are tight in TRPV1 and TRPV2 channels so that each subunit (VSLD and pore) can move as an independent unit. In Kv, the mobile S4 of VSD does not interact tightly with the pore domain (Fig. 7). Second, in order to maintain the high K^+ selectivity, K_V channels are rigidly structured around the SF, the pore helix, pore loop, S5 and S6 which prevents them from entering conformations with reduced symmetry. Similarly, the crystal structures of the Ca^{2+}-selective TRPV6 channel, in which the SF does not act as a gate, revealed a tight network of interactions around the SF which could explain why TRPV6 has only been captured in C4-symmetric conformations [37,41]. By contrast, the non-selective TRPV1 and TRPV2 channels possess more flexibility around the SF gate which renders them capable of adopting two-fold symmetric pore arrangements (Figure 7).

Our structural and functional studies illustrate the plasticity within the TRPV2 channel that enables permeation of large cations, and show that this plasticity originates from the diverse conformations of the S4-S5 linker that dictates the quaternary structure of the channel.

Methods

Expression and purification

The miTRPV2 construct was prepared as previously described. In brief, the codon-optimized gene for the full-length rabbit TRPV2 was synthesized and the truncated construct, miTRPV2, containing residues 57–561 and 583–722 was cloned into a pFastBac vector with a C-terminal FLAG affinity tag. Baculovirus was produced according to manufacturers' protocol (Invitrogen, Bac-to-Bac). To obtain the miTRPV2$_{QM}$ construct, point mutations F470S, L505M, L508T and Q528E were introduced to the miTRPV2. For protein expression, Sf9 insect cells were infected with baculovirus at a density of 1.3M cells ml^{-1} and grown at 27 °C for 72 hours in an orbital shaker. After 72 hours, cell pellets were collected, resuspended in buffer A (50 mM TRIS pH8, 150 mM NaCl, 2 mM $CaCl_2$, 1 µg ml^{-1} leupeptin, 1.5 µg ml^{-1} pepstatin, 0.84 µg ml^{-1} aprotinin, 0.3 mM PMSF, 14.3 mM β-mercapto ethanol, and DNAseI) and broken by sonication (3×30 pulses).

miTRPV2 was prepared for crystallization as follows: 40mM Dodecyl β-maltoside (DDM, Anatrace) and 4mM Cholesteryl Hemmisuccinate Tris salt (CHS, Anatrace) were added to

the lysate for extraction at 4 °C for 1 hour. Insoluble material was removed by centrifugation (8,000g, 30 minutes), and anti-FLAG resin was added to the supernatant for 1 hour at 4 °C.

After incubation, the resin was loaded onto a Bio-Rad column and washed with Buffer B (50 mM TRIS pH8, 150 mM NaCl, 2 mM $CaCl_2$, 0.1 mM Decyl Maltoside Neopentyl Glycol (DMNG, Anatrace), 0.1 mM CHS, 0.1mg ml^{-1} 1,2-dimyristoyl-*sn*-glycero-3-phosphocholine (DMPC, Avanti Polar Lipids), 10 mM DTT) before being eluted in 5 column volumes buffer C (50 mM TRIS pH8, 150 mM NaCl, 2 mM $CaCl_2$, 0.1 mM DMNG, 0. 1mM CHS, 0.1 mg ml^{-1} DMPC, 10 mM DTT, 0.1 mg ml^{-1} FLAG peptide). The eluate was incubated over night at 4 °C with 3 mM Tris(2-carboxyethyl)phosphine hydrochloride (TCEP, Sigma Aldrich) and PreScission protease.

Selenomethionine labelled miTRPV2 protein was expressed using ESF 921 Delta Series methionine deficient Sf9 insect cell media (Expression Systems) according to the manufacturer's protocol. In brief, the Sf9 cells adapted to the methionine deficient media were grown up to a density of 0.7 M ml^{-1} and infected with baculovirus. 24 hours following infection, 100 mg ml^{-1} L-selenomethionine (Sigma Aldrich) was added and the cells were grown for another 48 hours at 27 °C. The cell pellets were harvested by centrifugation and the protein prepared as described for miTRPV2, except without β-mercaptoethanol and DTT addition.

The miTRPV2$_{QM}$ protein was extracted with 20 mM Octyl Glucose Neopentyl Glycol (OGNG, Anatrace) and 2 mM CHS in the presence of 2 μM RTx (Sigma Aldrich) for 1 hour at 4 °C. Following removal of insoluble matter by centrifugation (8,000g, 30 minutes), the extract was loaded onto anti-FLAG affinity resin and incubated for 1 hour at 4 °C.

The resin was washed with 10xCV buffer B$_{RTx}$ (50 mM TRIS pH8, 150 mM NaCl, 2 mM $CaCl_2$, 2 mM OGNG, 0.2 mM CHS, 0.1 mg ml^{-1} DMPC, 2 μM RTx, 10 mM DTT) and the protein eluted in buffer C$_{RTx}$ (50 mM TRIS pH8, 150 mM NaCl, 2 mM $CaCl_2$, 2 mM OGNG, 0.2 mM CHS, 0.1 mg ml^{-1} DMPC, 2 μM RTx, 10 mM DTT, 0.1 mg ml^{-1} FLAG peptide). The eluate was incubated over night at 4 °C with PreScission protease and 3 mM TCEP, before being subjected to gel filtration on a Superose 6 column.

Crystallization, structure determination and refinement

Following size exclusion chromatography on a Superose 6 column (GE Healthcare), the miTRPV2 protein peak was collected and concentrated to 8–10 mg ml^{-1}, supplemented with 5mM TCEP and mixed with crystallization solution at a 1:1 ratio in 96-well sitting drop plates. The miTRPV2$_{QM}$ protein peak was collected, concentrated to 8–10 mg ml^{-1} and supplemented with 300 μM RTx and 5mM TCEP before being mixed with crystallization solution at a 1:1 ratio in 96-well sitting drop plates. Crystals of both proteins were obtained in many conditions, but the best diffracting ones grew in 200–400 mM $CaCl_2$, 15–25% PEG400 at pH 7–9. The crystals were incubated at 17 °C for up to two weeks, and transferred to 4 °C 24 hours before harvest, after which they were coated in a cryo-protective solution containing 36% PEG400 and flash frozen in liquid nitrogen.

Data were collected at Advanced Photon Source beam lines 22-ID, 24-ID-C and 24-ID-E and processed using XDS. Because the crystals of both miTRPV2$_{Ca^{2+}}$ and miTRPV2$_{RTx,Ca^{2+}}$ were highly isomorphous, we were able to merge data from multiple crystals using BLEND [42] in order to increase redundancy and extend the resolution to 3.9 Å and 3.1 Å respectively. Four data sets were merged to produce the final miTRPV2$_{Ca^{2+}}$ data set and two were merged to generate the final data set for miTRPV2$_{RTx,Ca^{2+}}$.

Furthermore, we employed BLEND to merge 10 data sets of the selenomethionine labelled miTRPV2$_{Ca^{2+}}$ crystals in order to increase the anomalous signal. This data was used to confirm the position of methionine residues in the 3.9 Å miTRPV2 structure.

Phases were obtained through molecular replacement using PHASER [43] where fragments of the previously determined TRPV2 structure (PDB ID 5an8) (ARD (residues 70–320) and TM (residues 387–670)) were employed as ensemble search models. The resulting maps enabled interpretation and model building in Coot [44]. Composite omit maps were created using Phenix [45] in order to verify the positions of transmembrane helices and ligands. The quality of the map for the miTRPV2$_{Ca^{2+}}$ allowed us to build the backbone of residues 70–558, 590–604 and 616–727 of both chains in the ASU. The ARD region was well resolved and allowed building of most side chains. The transmembrane regions (residues 387–647) were more poorly defined, but the electron density allowed for building of most bulky side chains. The map quality for the miTRPV2$_{RTx,Ca^{2+}}$ was considerably better, and allowed most side chains to be built for residues 70–558, 586–606, 614–727 in chain A and 70–558, 586–612, 614–727 in chain B. The refinement was performed using Phenix [45] The final miTRPV2$_{Ca^{2+}}$ model was refined to R_{work}/R_{free} 25.4/28.2, good geometry (96.3% Ramachandran favoured, 0.83% Ramachandran outliers) and a Molprobity score of 1.6. The miTRPV2$_{RTx,Ca^{2+}}$ was refined to R_{work}/R_{free} 24.2/27.1 with 93.6% occupying the favored positions in the Ramachandran plot and 0.53% outliers, and a Molprobity score of 1.7.

Structure Alignments and Analysis

Tetrameric assemblies for both miTRPV2$_{Ca^{2+}}$ and miTRPV2$_{RTx,Ca^{2+}}$ were generated in Coot. The miTRPV2$_{Ca^{2+}}$ and miTRPV2$_{EM}$ structures were aligned via residues 387–403, 438–446, 474–482 and 503–510 of subunits A and C. miTRPV2$_{Ca^{2+}}$ and miTRPV2$_{RTx,Ca^{2+}}$ were aligned via residues 387–403, 438–446, 474–482 and 503–510 of subunits B and D. To determine the extent and origin of subunit rotation, separate pdb files were generated for subunit A of miTRPV2$_{Ca^{2+}}$ and miTRPV2$_{RTx,Ca^{2+}}$ which merged residues 387–517 of chain A and 518–647 of chain B into a single chain. These pdb files were analysed using DynDom [46] in the CCP4 suite [47]. Distances and angles were measured in Coot and Pymol [48]. All structure illustrations were prepared using Pymol.

Cell culture and transfection

HEK293T cells, tested negative for mycoplasma by Duke Cell Culture Facility, were grown in DMEM supplemented with 10% FBS (Sigma), 1% penicillin and streptomycin (Gibco) and supplied with 5% CO_2 at 37°C. Cells were grown in 35 mm 6-well plates until reaching 40–60% confluency and transiently transfected using X-tremeGENE 9 DNA transfection reagent (Sigma). For whole-cell and inside-out recordings, 3 μg of plasmid encoding rabbit TRPV2 and 0.5 μg cDNA encoding EGFP were used at a 1:2 DNA:reagent ratio. For YO-PRO-1 uptake experiments, 0.5μg cDNA encoding mCherry was used for identification of transfected cells. 24 hours after transfection, cells were trypsinized and reseeded onto round glass coverslips (Assistent) precoated with Poly-D-Lysine (PDL, Sigma) and laminin (Sigma). Both electrophysiology recordings and YO-PRO-1 uptake imaging experiments were performed approximately 48 hours following transfection.

Electrophysiology

All electrophysiology recordings were done at room temperature. Whole-cell patch clamp recordings were performed on isolated GFP-positive cells with borosilicate glass electrodes with a resistance of 2–3 MΩ (Sutter Instrument). The internal pipette solution contained 150 mM NaCl, 3 mM $MgCl_2$, 5 mM EGTA and 10 mM HEPES, adjusted to pH 7.2 (NaOH), and the bath solution contained 150 mM NaCl, 6 mM CsCl, 1.5 mM $CaCl_2$, 1 mM $MgCl_2$, 10 mM glucose and 10 mM HEPES, adjusted to pH 7.4 (NaOH). For inside-out recordings, borosilicate pipettes with a resistance of 1.5–2 MΩ were used, and the pipette solution (external solution) contained 150 mM NaCl, 5 mM EGTA, 10 mM HEPES, adjusted to pH 7.3 (NaOH). Extracellular and intracellular solution applications were performed using a microperfusion system (ALA Scientific Instruments) in which the perfusion outlet was directly positioned close to the patched cell after whole-cell configuration was established or in front of the pipette tip with the excised membrane patch. Channel activation was triggered by application of either 50 nM resiniferatoxin (RTx, Sigma) or 2 mM 2-Aminoethoxydiphenyl borate (2-APB, Sigma). Current responses were elicited by a continuous 500 ms ramp protocol from −120 mV to +120 mV with a holding potential of 0 mV at 5 second intervals. Data were low-pass filtered at 5kHz (Axopatch 200B) and digitally sampled at 10 kHz (Axon Digidata 1550A) controlled by Clampex 10 and analyzed by Clampfit 10 (Molecular Devices) and Microsoft Excel (Microsoft).

For the reversal potential measurement experiments, inside-out configuration was used for easy exchange of the intracellular solution (bath solution). The pipette solution (external solution) contained 150 mM NaCl, 5 mM EGTA, 10 mM HEPES, adjusted to pH 7.3 (NaOH). The TRPV2 channels in the excised patch were activated by perfusion of 50nM RTx in a bath solution containing 150 mM NaCl, 5 mM EGTA, 10 mM HEPES, adjusted to pH 7.3 (NaOH) using a ramp protocol from −120mV to +120mV. Once the channel activity stabilized, the intracellular solution (bath solution) was rapidly switched to a solution containing 150 mM NMDG-Cl, 5 mM EGTA, 10 mM HEPES, adjusted to pH 7.3 (NaOH) using a microperfusion system (ALA Scientific Instruments). The reversal potential (E_{rev}) after intracellular Na^+ was exchanged with equimolar $NMDG^+$ was determined by measuring the voltage at which the current was zero, and five consecutive $NMDG^+$ current

traces were averaged for each recording. The shift in E_{rev} was calculated by subtracting the E_{rev} of $NMDG^+$ from the E_{rev} measured in symmetrical Na^+.

The permeability ratio P_{NMDG^+}/P_{Na^+} was calculated using the equation:

$$P_{NMDG^+}/P_{Na^+} = [Na^+]_{ext}/([NMDG^+]_{int} \cdot \exp(\Delta E_{rev}F/RT))$$

where ΔE_{rev} is the measured reversal potential shift, F is the Faraday's constant (96485 C mol^{-1}), R is the gas constant (8.314 J mol^{-1}), T is the absolute temperature (298.15 K at 25 °C), and $[Na^+]_{ext}$ and $[NMDG^+]_{int}$ are the concentrations (in mM) of extracellular Na^+ and intracellular $NMDG^+$, respectively.

YO-PRO-1 dye uptake assay

YO-PRO-1 dye uptake experiments were done at room temperature. Transfected cells reseeded on PDL and laminin-coated glass coverslips were washed twice with Dulbecco's Phosphate Buffered Saline (DPBS, Sigma) containing 0.2 mM KCl, 0.2 mM KH_2PO_4, 8 mM NaCl, 1.15 mM Na_2HPO_4. Washed cells were incubated for 5 minutes at 37°C in 10 μM YO-PRO-1 imaging solution made from diluting 1 mM YO-PRO-1 DMSO stock solution (ThermoFisher) in DPBS. YO-PRO-1 uptake was triggered by addition of 250 nM RTx. Time-dependent YO-PRO-1 uptake by mCherry-positive cells was monitored by an inverted fluorescence microscope (IX73, Olympus America Inc.) using an FITC channel (excitation wavelength 470/40 nm; emission wavelength 525/50 nm). Images were acquired by a CMOS camera (Prime 95b, Photometrics) at 5 second intervals. MetaMorph software (Molecular Devices) was used to control the fluorophore excitation and image acquisition. MATLAB software (MathWorks) was used to analyze the time-dependent increase in YO-PRO-1 uptake.

Data availability statement

The sequence of rabbit TRPV2 can be found in the National Center for Biotechnology Information (accession code XM_017349044). The coordinates are deposited in the Protein Data Bank under PDB ID 6BWJ and 6BWM. Source data for all electrophysiology and fluorescence imaging experiments (figures 1c–d, 4a–d, 5d–i, 6b–f and supplementary figures 2a–h and 8a–d) are available with the paper online.

Supplementary Material

Refer to Web version on PubMed Central for supplementary material.

Acknowledgments

References

1. Ramsey IS, Delling M, Clapham DE. An introduction to TRP channels. Annu Rev Physiol. 2006; 68:619–647. [PubMed: 16460286]

2. Julius D. TRP channels and pain. Annu Rev Cell Dev Biol. 2013; 29:355–384. [PubMed: 24099085]

3. Nilius B, Voets T. TRP channels: a TR(I)P through a world of multifunctional cation channels. Pflugers Arch. 2005; 451:1–10. [PubMed: 16012814]

4. Venkatachalam K, Montell C. TRP channels. Annu Rev Biochem. 2007; 76:387–417. [PubMed: 17579562]

5. Dhaka A, Viswanath V, Patapoutian A. TRP Ion Channels and Temperature Sensation. Annu Rev Neurosci. 2006

6. Liu B, Qin F. Use Dependence of Heat Sensitivity of Vanilloid Receptor TRPV2. Biophys J. 2016; 110:1523–1537. [PubMed: 27074678]

7. Caterina MJ, et al. The capsaicin receptor: a heat-activated ion channel in the pain pathway. Nature. 1997; 389:816–824. [PubMed: 9349813]

8. Long SB, Campbell EB, Mackinnon R. Crystal structure of a mammalian voltage-dependent Shaker family K+ channel. Science. 2005; 309:897–903. [PubMed: 16002581]

9. Lenaeus MJ, et al. Structures of closed and open states of a voltage-gated sodium channel. Proceedings of the National Academy of Sciences of the United States of America. 2017; 114:E3051–E3060. [PubMed: 28348242]

10. Holmgren M, Shin KS, Yellen G. The activation gate of a voltage-gated K+ channel can be trapped in the open state by an intersubunit metal bridge. Neuron. 1998; 21:617–621. [PubMed: 9768847]

11. Yellen G. The moving parts of voltage-gated ion channels. Q Rev Biophys. 1998; 31:239–295. [PubMed: 10384687]

12. Hackos DH, Chang TH, Swartz KJ. Scanning the intracellular S6 activation gate in the shaker K+ channel. J Gen Physiol. 2002; 119:521–532. [PubMed: 12034760]

13. Xie C, Zhen XG, Yang J. Localization of the activation gate of a voltage-gated Ca2+ channel. J Gen Physiol. 2005; 126:205–212. [PubMed: 16129771]

14. Cao E, Liao M, Cheng Y, Julius D. TRPV1 structures in distinct conformations reveal activation mechanisms. Nature. 2013; 504:113–118. [PubMed: 24305161]

15. Munns CH, Chung MK, Sanchez YE, Amzel LM, Caterina MJ. Role of the outer pore domain in transient receptor potential vanilloid 1 dynamic permeability to large cations. The Journal of biological chemistry. 2015; 290:5707–5724. [PubMed: 25568328]

16. Chung MK, Guler AD, Caterina MJ. TRPV1 shows dynamic ionic selectivity during agonist stimulation. Nat Neurosci. 2008; 11:555–564. [PubMed: 18391945]

17. Puopolo M, et al. Permeation and block of TRPV1 channels by the cationic lidocaine derivative QX-314. J Neurophysiol. 2013; 109:1704–1712. [PubMed: 23303863]

18. Chen J, et al. Pore dilation occurs in TRPA1 but not in TRPM8 channels. Mol Pain. 2009; 5:3. [PubMed: 19159452]

19. Ferreira LG, Faria RX. TRPing on the pore phenomenon: what do we know about transient receptor potential ion channel-related pore dilation up to now? J Bioenerg Biomembr. 2016; 48:1–12. [PubMed: 26728159]

20. Nabissi M, Morelli MB, Santoni M, Santoni G. Triggering of the TRPV2 channel by cannabidiol sensitizes glioblastoma cells to cytotoxic chemotherapeutic agents. Carcinogenesis. 2013; 34:48–57. [PubMed: 23079154]

21. Banke TG, Chaplan SR, Wickenden AD. Dynamic changes in the TRPA1 selectivity filter lead to progressive but reversible pore dilation. Am J Physiol Cell Physiol. 2010; 298:C1457–C1468. [PubMed: 20457836]

22. Li H, Wang S, Chuang AY, Cohen BE, Chuang HH. Activitydependent targeting of TRPV1 with a pore-permeating capsaicin analog. Proc Natl Acad Sci USA. 2011; 108:8497–8502. [PubMed: 21536874]

23. Li M, Toombes GE, Silberberg SD, Swartz KJ. Physical basis of apparent pore dilation of ATP-activated P2X receptor channels. Nat Neurosci. 2015; 18:1577–1583. [PubMed: 26389841]

24. Samways DS, Tomkiewicz E, Langevin OM, Bukhari M. Measurement of relative Ca(2)(+) permeability during sustained activation of TRPV1 receptors. Pflugers Arch. 2016; 468:201–211. [PubMed: 26490461]

25. Brenneis C, et al. Bupivacaine-induced cellular entry of QX-314 and its contribution to differential nerve block. Br J Pharmacol. 2014; 171:438–451. [PubMed: 24117225]

26. Binshtok AM, et al. Coapplication of lidocaine and the permanently charged sodium channel blocker QX-314 produces a long-lasting nociceptive blockade in rodents. Anesthesiology. 2009; 111:127–137. [PubMed: 19512868]

27. Bean BP. Pore dilation reconsidered. Nat Neurosci. 2015; 18:1534–1535. [PubMed: 26505561]

28. Zhou M, Morais-Cabral JH, Mann S, MacKinnon R. Potassium channel receptor site for the inactivation gate and quaternary amine inhibitors. Nature. 2001; 411:657–661. [PubMed: 11395760]

29. Choi KL, Aldrich RW, Yellen G. Tetraethylammonium blockade distinguishes two inactivation mechanisms in voltage-activated K+ channels. Proceedings of the National Academy of Sciences of the United States of America. 1991; 88:5092–5095. [PubMed: 2052588]

30. Mitcheson JS, Chen J, Lin M, Culberson C, Sanguinetti MC. A structural basis for drug-induced long QT syndrome. Proceedings of the National Academy of Sciences of the United States of America. 2000; 97:12329–12333. [PubMed: 11005845]

31. Liao M, Cao E, Julius D, Cheng Y. Structure of the TRPV1 ion channel determined by electron cryo-microscopy. Nature. 2013; 504:107–112. [PubMed: 24305160]

32. Zubcevic L, et al. Cryo-electron microscopy structure of the TRPV2 ion channel. Nature structural & molecular biology. 2016

33. Huynh KW, et al. Structure of the full-length TRPV2 channel by cryo-EM. Nature communications. 2016; 7:11130.

34. Zhang F, et al. Engineering vanilloid-sensitivity into the rat TRPV2 channel. Elife. 2016; 5

35. Yang F, Vu S, Yarov-Yarovoy V, Zheng J. Rational design and validation of a vanilloid-sensitive TRPV2 ion channel. Proceedings of the National Academy of Sciences of the United States of America. 2016; 113:E3657–3666. [PubMed: 27298359]

36. Gao Y, Cao E, Julius D, Cheng Y. TRPV1 structures in nanodiscs reveal mechanisms of ligand and lipid action. Nature. 2016; 534:347–351. [PubMed: 27281200]

37. McGoldrick LL, et al. Opening of the human epithelial calcium channel TRPV6. Nature. 2018; 553:233–237. [PubMed: 29258289]

38. Chugunov AO, Volynsky PE, Krylov NA, Nolde DE, Efremov RG. Temperature-sensitive gating of TRPV1 channel as probed by atomistic simulations of its trans- and juxtamembrane domains. Sci Rep. 2016; 6:33112. [PubMed: 27612191]

39. Matthies D, et al. Cryo-EM Structures of the Magnesium Channel CorA Reveal Symmetry Break upon Gating. Cell. 2016; 164:747–756. [PubMed: 26871634]

40. Hite RK, MacKinnon R. Structural Titration of Slo2.2, a Na+-Dependent K+ Channel. Cell. 2017; 168:390–399e311. [PubMed: 28111072]

41. Saotome K, Singh AK, Yelshanskaya MV, Sobolevsky AI. Crystal structure of the epithelial calcium channel TRPV6. Nature. 2016; 534:506–511. [PubMed: 27296226]

42. Foadi J, et al. Clustering procedures for the optimal selection of data sets from multiple crystals in macromolecular crystallography. Acta crystallographica. Section D, Biological crystallography. 2013; 69:1617–1632. DOI: 10.1107/S0907444913012274 [PubMed: 23897484]

43. McCoy AJ, et al. Phaser crystallographic software. J Appl Crystallogr. 2007; 40:658–674. DOI: 10.1107/S0021889807021206 [PubMed: 19461840]

44. Emsley P, Cowtan K. Coot: model-building tools for molecular graphics. Acta crystallographica. Section D, Biological crystallography. 2004; 60:2126–2132. S0907444904019158. [PubMed: 15572765]

45. Adams PD, et al. PHENIX: a comprehensive Python-based system for macromolecular structure solution. Acta crystallographica. Section D, Biological crystallography. 2010; 66:213–221. S0907444909052925. [PubMed: 20124702]

46. Hayward S, Lee RA. Improvements in the analysis of domain motions in proteins from conformational change: DynDom version 1.50. J Mol Graph Model. 2002; 21:181–183. [PubMed: 12463636]

47. Winn MD, et al. Overview of the CCP4 suite and current developments. Acta crystallographica. Section D, Biological crystallography. 2011; 67:235–242. DOI: 10.1107/S0907444910045749 [PubMed: 21460441]

48. Delano, WL. The PyMol Molecular Graphics System. DeLano Scientific; 2002.
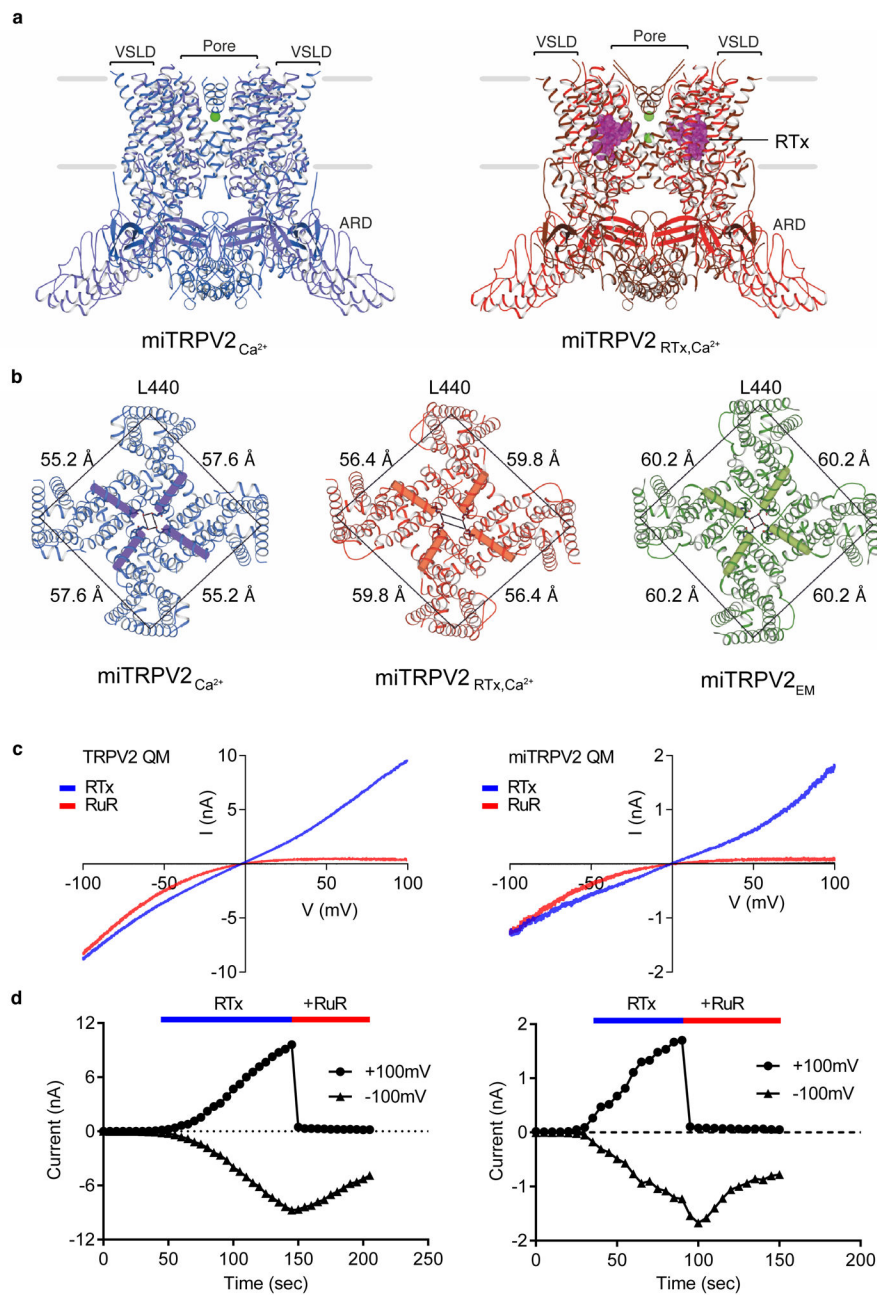
Figure 1. Overview of miTRPV2$_{Ca^{2+}}$ **and** miTRPV2$_{RTx,Ca^{2+}}$ **and functional characterization of the constructs**

a, Left panel, side view of the miTRPV2$_{Ca^{2+}}$ tetramer with chains colored in alternately in marine and slate. A putative calcium ion is represented as a green sphere. Right panel, side view of the miTRPV2$_{RTx,Ca^{2+}}$ tetrameric assembly. Chains are colored alternately in red and chocolate brown. The RTx molecule is shown in sphere representation and colored magenta. The putative calcium ions are shown as green spheres. **b,** Top view comparison of channel

dimensions and symmetry in $miTRPV2_{EM}$ (green), $miTRPV2_{Ca^{2+}}$ (blue), $miTRPV2_{RTx,Ca^{2+}}$ (red). The lines are drawn between Cα atoms of Gly604 in the selectivity filter and Leu440 in S2 (distances shown). Pore helices are shown both in helix and cylinder representation. Ankyrin repeat domains were removed for clarity. **c,** Representative current-voltage relationships of $TRPV2_{QM}$ (n=10) and $miTRPV2_{QM}$ (n=7) from inside-out patch recordings in response to RTx before (blue) and after (red) application of ruthenium red (RuR). **d,** Time-course of RTx-evoked currents of $TRPV2_{QM}$ and $miTRPV2_{QM}$ elicited by a repeated ramp protocol (circles, +100 mV; triangles, −100 mV) at 5s intervals. Blue and red bars depict application of 50 nM RTx alone and co-application of 50 nM RTx and 200 μM ruthenium red, respectively.
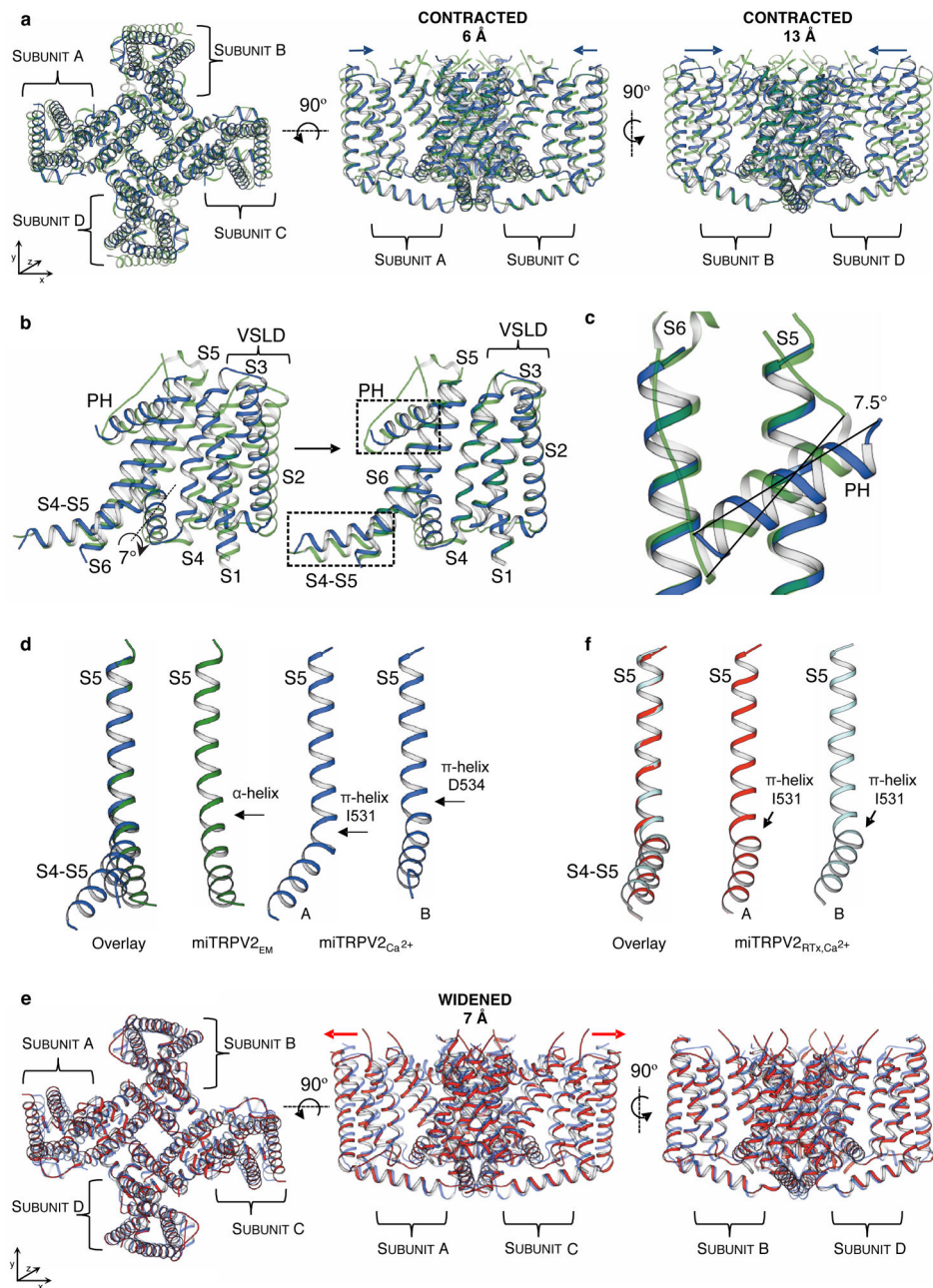
Figure 2. π-helices in the S4-S5 linker determine the quaternary structure of subunits and conformation of the pore helices

a, Alignment of miTRPV2$_{Ca^{2+}}$ (marine) and miTRPV2$_{EM}$ (green). The ankyrin repeat domains were removed for clarity. Top view of the channel (left) illustrates the overall differences in dimensions in the two structures. A side view of subunits A and C (middle) illustrates a contraction measured to 6 Å while the contraction between subunits B and D (right) was measured to 13 Å (Cα distance between residues Asn429 in opposing subunits, not shown). **b,** A 7° rotation of the miTRPV2$_{Ca^{2+}}$ subunit B around the S4-S5 linker is

sufficient to achieve alignment with the subunit B of the miTRPV2$_{EM}$ (Cα r.m.s.d. ~0.75 Å). The dashed line represents the rotation axis. **c,** Pore helices of the aligned subunits of miTRPV2$_{Ca^{2+}}$ and miTRPV2$_{EM}$ are positioned at different angles. **d,** Alignment of S5 helices of subunits A and B of the miTRPV2$_{Ca^{2+}}$ structure illustrates that their S4-S5 linkers diverge significantly from each other. **e,** Alignment of miTRPV2$_{RTx,Ca^{2+}}$ (red) and miTRPV2$_{Ca^{2+}}$ (marine). Top view of the alignment (left) shows that subunits A and C of the miTRPV2$_{RTx,Ca^{2+}}$ are widened with respect to miTRPV2$_{Ca^{2+}}$, and that their pore helices are significantly displaced. Side view of subunits A and C (middle) show the extent of the widening (7 Å difference in Cα distance from Asn429 of subunit A to subunit C). **f,** Overlay of the subunit A (red) and B (pale cyan) S5 helices of miTRPV2$_{RTx,Ca^{2+}}$ indicates a significant difference in the S4-S5 linker conformations in the two subunits.
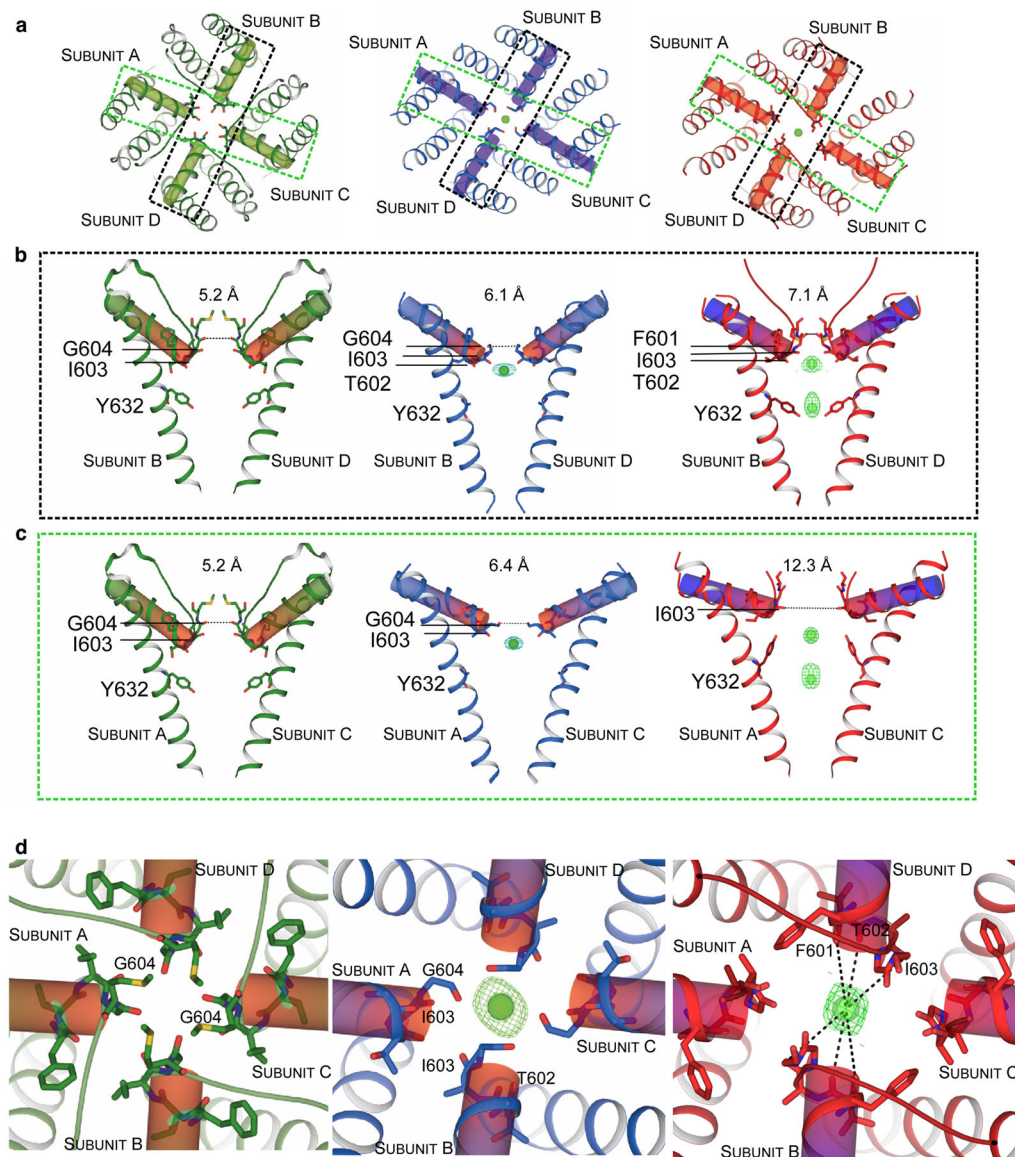
Figure 3. Comparison of miTRPV2$_{EM}$, miTRPV2$_{Ca^{2+}}$ and miTRPV2$_{RTx,Ca^{2+}}$ pores

a, A close up of the top view of the miTRPV2$_{EM}$ (green), miTRPV2$_{Ca^{2+}}$ (blue),

miTRPV2$_{RTx,Ca^{2+}}$ (red) channels, showing S5, S6 and pore helices. The pore helices are

drawn in both helix and cylinder representation. A black box indicates subunits B and D, while the green box indicates subunits A and C. **b,** S6 and pore helices of subunits B and D. S6 is shown in cartoon representation, and pore helices are shown in both cylinder and cartoon representation. The cylinders are colored to indicate the helical dipoles. Dashes and values represent distances across the selectivity filter. Calcium ions are shown as green spheres with 2F$_o$-F$_c$ density contoured at 1–1.3 σ. **c,** S6 and pore helices of subunits A and C. **d,** Top view of the pore in miTRPV2$_{EM}$ (left, green), miTRPV2$_{Ca^{2+}}$ (middle, marine) and
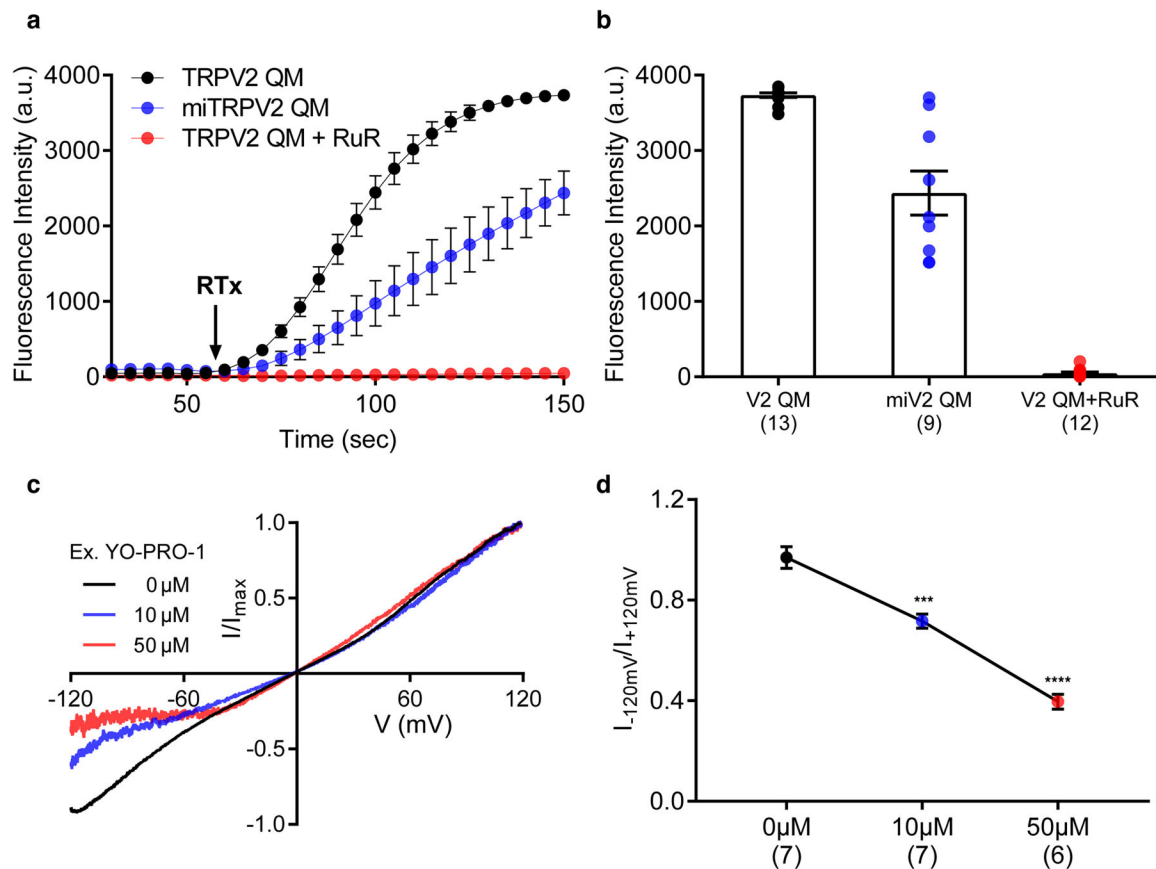
miTRPV2$_{RTx,Ca^{2+}}$ (right, red). Residues 601-605 are shown in stick representation. The dashed lines show calcium ion coordination in the selectivity filter of miTRPV2$_{RTx,Ca^{2+}}$.

Figure 4. TRPV2$_{QM}$ permeates YO-PRO-1 through the ion permeation pathway

a,b, YO-PRO-1 dye uptake by HEK293T cells expressing TRPV2$_{QM}$, miTRPV2$_{QM}$ and TRPV2$_{QM}$ with 50 μM extracellular ruthenium red (**a**) and their peak fluorescence intensities (**b**). YO-PRO-1 uptake was triggered by addition of 250 nM RTx (black arrow). TRPV2 expressing cells (identified by cotransfected mCherry) from 3 repeats of imaging experiments were chosen for analysis and the total number of cells analyzed are noted in parentheses. **c**, Representative RTx-evoked TRPV2$_{QM}$ current traces from inside-out patches in the presence of extracellular 0 μM, 10 μM or 50 μM YO-PRO-1 in the pipette solution. Currents were normalized to the peak amplitudes at +120 mV. **d**, Extracellular YO-PRO-1 attenuates the TRPV2$_{QM}$ inward currents as quantified by the ratios of peak current amplitudes at −120 mV and +120 mV. The number of patches is noted in parentheses. Data are presented as mean ± s.e.m. (***p<0.001 and ****p<0.0001, two-tailed unpaired Student's t-test. p-values: 0.0003 for 10 μM and p<0.0001 for 50 μM YO-PRO-1).
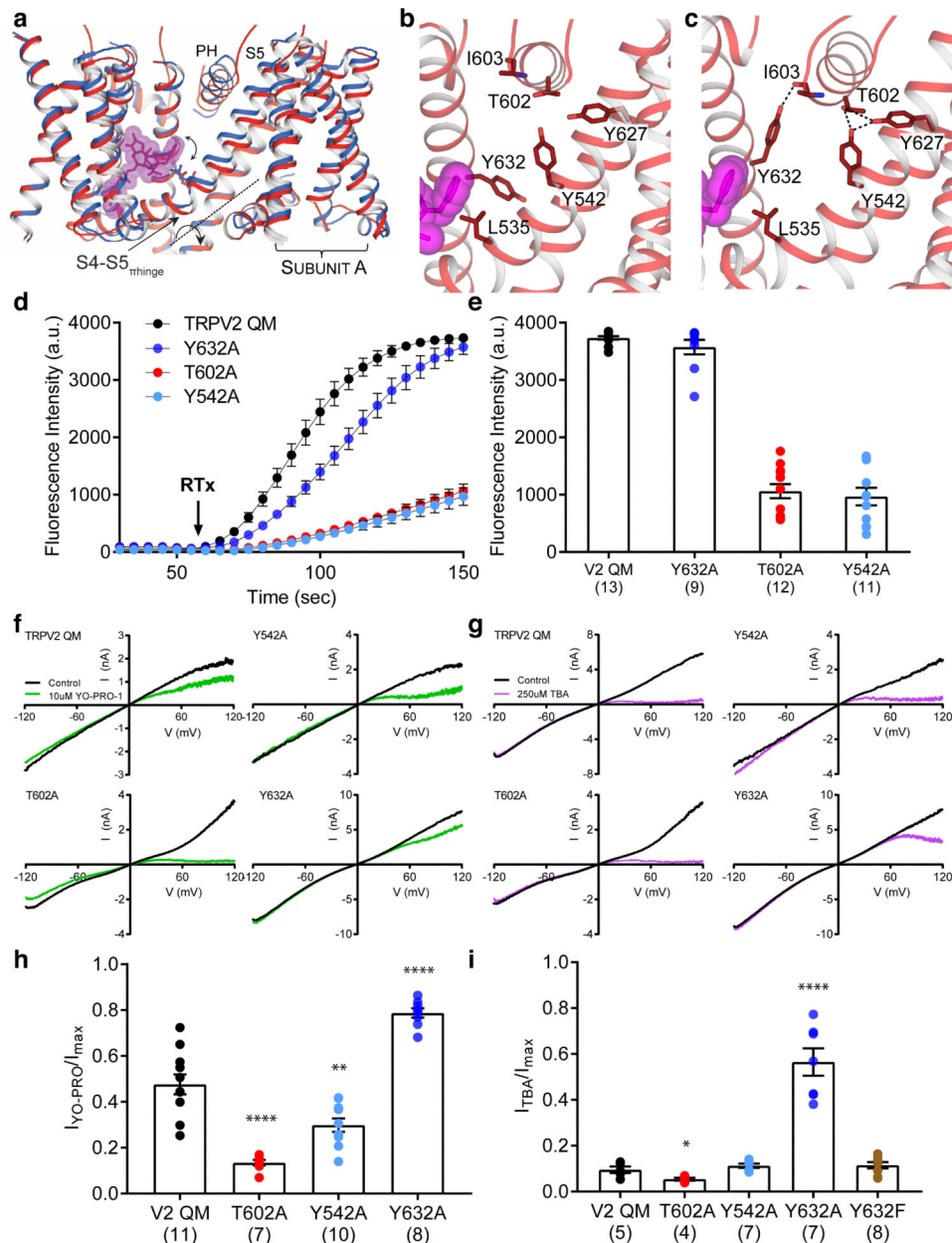
Figure 5. The importance of the hydrogen bond triad between PH and S5 in miTRPV2$_{RTx,Ca^{2+}}$

in YO-PRO-1 permeation

a, Side view of the overlay of the miTRPV2$_{Ca^{2+}}$ (marine) and miTRPV2$_{RTx,Ca^{2+}}$ (red)

subunits D and A, with RTx shown in stick and sphere representation and colored in

magenta. Binding of RTx to the miTRPV2$_{Ca^{2+}}$ would push down on the S4-S5 linker π-

hinge (rotation plane indicated by dashed line) and force the subunit A to rotate. **b,** A side

view of the hydrogen bond triad in the widened subunit A. **c,** Side view of the hydrogen

bond triad in the contracted subunit B. In addition, residue Tyr632 from the neighboring

subunit forms a hydrogen bond with the backbone carbonyl of Ile603 in the pore helix. **d, e,**

YO-PRO-1 dye uptake by HEK293T cells expressing TRPV2$_{QM}$, Tyr542Ala, Thr602Ala and Tyr632Ala (**d**) and their peak fluorescence intensities (**e**). YO-PRO-1 uptake was triggered by addition of 250 nM RTx (black arrow). **f, g,** Representative inside-out patch recordings from HEK293T cells expressing TRPV2$_{QM}$, Tyr542Ala, Thr602Ala and Tyr632Ala before and after intracellular application of 10 μM YO-PRO-1 (green trace in **f**) or 250 μM TBA (purple trace in **g**). **h, i**, Quantification of current inhibition by YO-PRO-1 (**h**) or TBA (**i**) of patches from cells expressing TRPV2$_{QM}$, Tyr542Ala, Thr602Ala and Tyr632Ala. The number of patches is noted in parentheses. Data are presented as mean ± s.e.m. *p<0.05, p**<0.01, ***p<0.001, ****p<0.0001, two-tailed unpaired Student's t-test. p-values for YO-PRO-1 experiments: 0.0035 for Tyr542Ala, p<0.0001 for Thr602Ala, p<0.0001 for Tyr632Ala. p-values for TBA experiments: 0.0481 for Thr602Ala, <0.0001 for Tyr632Ala, 0.2834 for Tyr542Ala, 0.355 for Tyr632Phe.
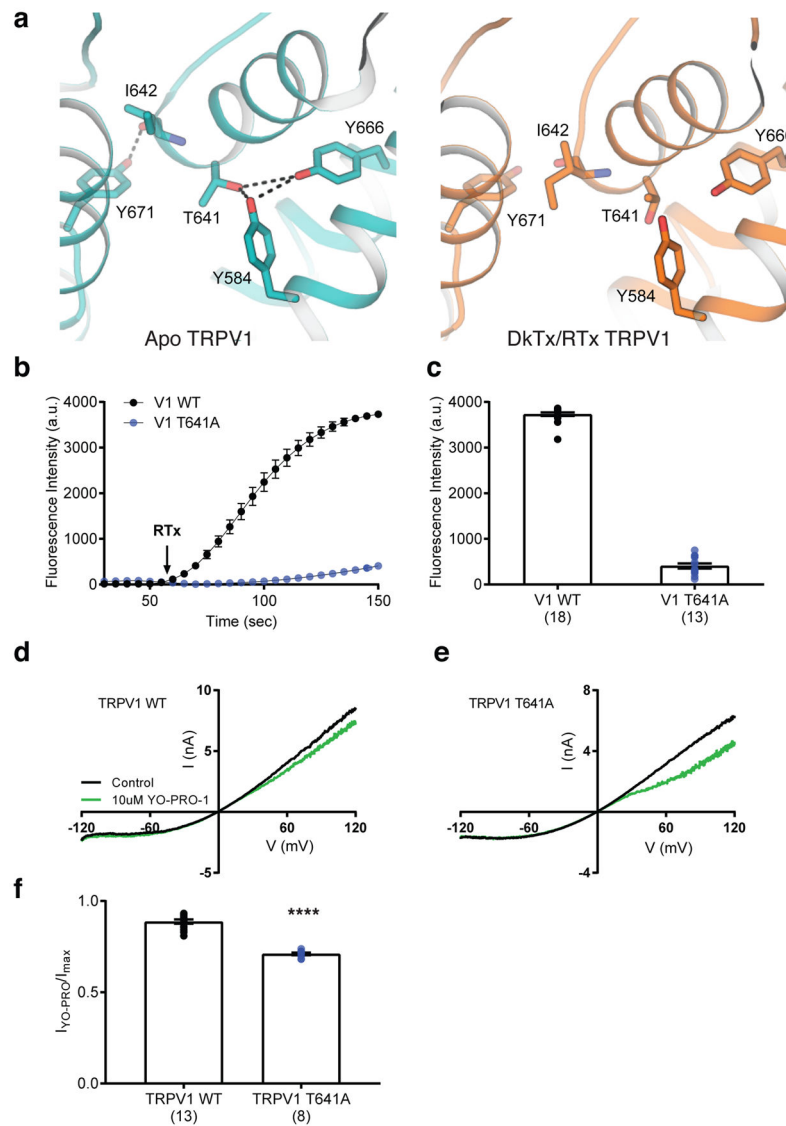
Figure 6. Functional characterization of the rat TRPV1 T641A mutant

a, Hydrogen bond networks around the pore of the closed TRPV1 channel (PDB ID 5IRZ). A tight network of hydrogen bonds is present at the Tyr584-Thr641-Tyr666 triad and between residues Tyr671 and Ile642. Hydrogen bonding is absent at the subunit interface of the DkTx-RTx bound TRPV1 channel (PDB ID 5IRX). **b, c,** YO-PRO-1 dye uptake by HEK293T cells expressing rat TRPV1 WT and TRPV1 Thr641Ala (**b**) and their peak fluorescence intensities (**c**). YO-PRO-1 uptake was triggered by addition of 250 nM RTx (black arrow). TRPV1 expressing cells (identified by cotransfected mCherry) from 3 repeats of imaging experiments were chosen for analysis and the total numbers are noted in parentheses. **d, e**, Representative inside-out recordings of TRPV1 WT (**d**) and TRPV1 Thr641Ala (**e**) (equivalent to the TRPV2 Thr602Ala) before (black trace) and after (green trace) intracellular application of 10 μM YO-PRO-1. **f**, Quantification of current inhibition by YO-PRO-1 of TRPV1 WT and TRPV1 Thr641Ala. Bar graphs and error bars denote mean ± s.e.m. $p < 0.0001$ for Thr641Ala, two-tailed unpaired Student's t-test.

Kvchim   TRPV2
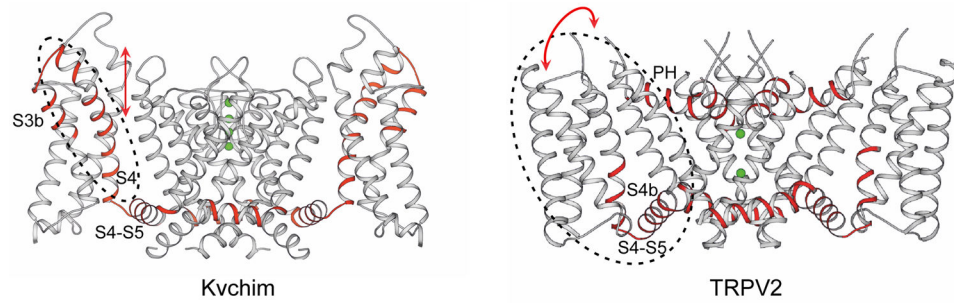
Figure 7. Comparison of flexible domains in K$_V$ and TRPV2 channels

K$_V$ (left), (K$_V$1.2–2.1 paddle chimera, PDB ID 2R9R) with the mobile regions, S3b, S4 and S4-S5 linker, colored in red. The arrow shows the motion of the mobile regions. The voltage sensing domain is able to move freely as it is not impeded by extensive interactions with the pore-forming domains. In TRPV2 (right) the VSLD is tightly coupled to the pore-forming domains. This makes independent movement of the VSLD unlikely, and instead we observe rotation of the entire subunit (dotted oval) which is dictated by the mobile regions (colored in red).

Table 1

Data collection and refinement statistics

	miTRPV2 Ca^{2+} [a] **PDB ID 6BWM**	miTRPV2 RTx,Ca^{2+} [b] **PDB ID 6BWJ**	miTRPV2 Ca^{2+} **SeMet**[c]
Data collection			
Space group	P 2 2₁ 2₁	P 2 2₁ 2₁	P 2 2₁ 2₁
Cell dimensions			
a, b, c (Å)	92.03, 122.36, 187.21	90.05, 121.22, 185.56	93.5, 125.39, 190.9
α, β, γ (°)	90, 90, 90	90, 90, 90	90, 90, 90
Resolution (Å)	39.85-3.9 (4.27-3.9)	45.03-3.1 (3.21-3.1)	48.51-5.0 (5.59 -5.0)
R_{pim}	0.19 (1.19)	0.16 (1.67)	0.1 (0.6)
$I/\sigma I$	8.8 (2.7)	8.6 (1.0)	11.4 (3.8)
$CC_{1/2}$	0.99 (0.85)	0.99 (0.33)	0.99 (0.89)
Completeness (%)	99.8 (99.6)	100 (100)	100 (100)
Redundancy	17.5 (17.8)	13.7 (13.7)	28.2 (28.5)
Refinement			
Resolution (Å)	39.85-3.9 (4.039-3.9)	45.03-3.1 (3.21-3.1)	
No. reflections	19867 (1930)	37513 (3639)	
R_{work}/R_{free}	0.25/0.29	0.24/0.27	
No. atoms	8508	18,363	
Protein	8507	18,189	
Ligand/ion	1 (Ca^{2+})	172 (RTx), 2 (Ca^{2+})	
B-factors			
Protein	103.37	86.58	
Ligand/ion	147.30	106.07	
R.m.s. deviations			
Bond lengths (Å)	0.002	0.005	
Bond angles (°)	0.55	0.73	

[a] Merged from 4 native miTRPV2 Ca^{2+} crystals

[b] Merged from 2 native miTRPV2 RTx,Ca^{2+} crystals

[c] Merged from 10 selenomethionine (SeMet) labelled miTRPV2 Ca^{2+} crystals